ACS APPLIED MATERIALS & INTERFACES

Research Article

www.acsami.org

Engineered Theranostic Magnetic Nanostructures: Role of Composition and Surface Coating on Magnetic Resonance Imaging Contrast and Thermal Activation

Vikas Nandwana,[†] Soo-Ryoon Ryoo,[†] Shanthi Kanthala,[†] Mrinmoy De,[‡] Stanley S. Chou,[§] Pottumarthi V. Prasad,[∥] and Vinayak P. Dravid*[,†]

[†]Department of Materials Science & Engineering, Northwestern University, Evanston, Illinois 60208, United States

[‡]Department of Organic Chemistry, Indian Institute of Science, Bengaluru, India

[§]Department of Electronic, Optical and Nano Materials, Sandia National Laboratory, Albuquerque, New Mexico 87185, United States

[∥]Department of Radiology, Northshore University Healthcare, Evanston, Illinois 60201, United States

Supporting Information

ABSTRACT: Magnetic nanostructures (MNS) have emerged as promising functional probes for simultaneous diagnostics and therapeutics (theranostic) applications due to their ability to enhance localized contrast in magnetic resonance imaging (MRI) and heat under external radio frequency (RF) field, respectively. We show that the "theranostic" potential of the MNS can be significantly enhanced by tuning their core composition and architecture of surface coating. Metal ferrite (e.g., MFe_2O_4) nanoparticles of ~8 nm size and nitrodopamine conjugated polyethylene glycol (NDOPA-PEG) were used as the core and surface coating of the MNS, respectively. The composition was controlled by tuning the stoichiometry of MFe_2O_4 nanoparticles (M = Fe, Mn, Zn, Zn_xMn_{1-x}) while the architecture of surface coating was tuned by changing the molecular weight of PEG, such that larger weight is expected to result in longer length extended away from the MNS surface. Our results suggest that both core as well as surface coating are important factors to take into consideration during the design of MNS as theranostic agents which is illustrated by relaxivity and thermal activation plots of MNS with different core composition and surface coating thickness. After optimization of these parameters, the r_2 relaxivity and specific absorption rate (SAR) up to 552 mM^{-1} s^{-1} and 385 W/g were obtained, respectively, which are among the highest values reported for MNS with core magnetic nanoparticles of size below 10 nm. In addition, NDOPA-PEG coated MFe_2O_4 nanostructures showed enhanced biocompatibility (up to [Fe] = 200 μg/mL) and reduced nonspecific uptake in macrophage cells in comparison to other well established FDA approved Fe based MR contrast agents.

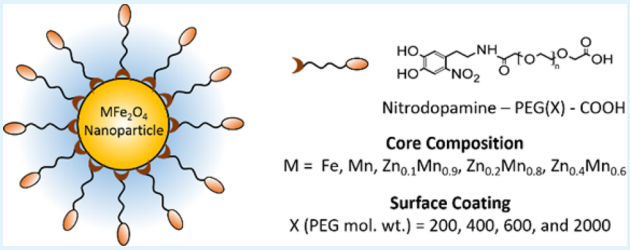

KEYWORDS: *magnetic nanostructures, theranostics, thermal activation, magnetic resonance imaging contrast, magnetic nanoparticles, biomedical applications, hyperthermia, nanomedicine*

INTRODUCTION

During the past decade, remarkable diagnostic and therapeutic advances have been made in nanomedicine, the field that originated through a combination of nanotechnology and biomedicine to address the challenges in conventional medicine.[1] A variety of nanostructures have been explored extensively due to the size similarity with biomolecules and their unique physical properties. In particular, magnetic nanostructures (MNS) have found significant attention due to their potential for "theranostic" applications, wherein MNS induced enhanced localized contrast in magnetic resonance imaging (MRI) can be utilized for diagnostics while the heat generation capability of MNS under external radio frequency (RF) field can be exploited for thermal therapy or actuated release of therapeutic cargo in bio/chemo/radio therapy.[2−6] A typical MNS architecture is composed of magnetic nanoparticle core and a surface coating. While the core provides theranostic properties, the coating provides stability, biocompatibility, and a surface amenable to functionalization for tagging targeting agents and bio/chemo/radio therapy cargo. MNS show superparamagnetic properties, which means they can be magnetized at very low magnetic fields (<0.5 T) but have no remanent magnetization in the absence of an applied magnetic field. Superparamagnetism is essential for biomedical studies since no remanent magnetization prevents their coagulation and sustains a long period of circulation in the body.

The theranostic properties of the MNS are characterized as r_2 relaxivity and specific absorption rate (SAR). Higher values of r_2 and SAR correspond to better contrast effect and thermal activation. In other words, higher r_2 and SAR values means low

Received: February 1, 2016
Accepted: March 2, 2016
Published: March 3, 2016

DOI: 10.1021/acsami.6b01377
ACS Appl. Mater. Interfaces 2016, 8, 6953−6961

dosage of theranostic administration is required. The theranostic properties of the core part of MNS have been tuned by controlling their size and composition.[7] Cheon et al.[8] have shown that by increasing the size from 4 to 12 nm, r_2 relaxivity of Fe_3O_4 nanoparticles can be increased from 78 to 218 mM^{-1} s^{-1}. Hyeon et al.[9] reported r_2 of 324 mM^{-1} s^{-1} by increasing the size of iron oxide nanocubes to 58 nm. De la Presa et al.[10] showed increase in SAR from 10 to 55 W/g with increasing Fe_3O_4 nanoparticles size from 8 to 13 nm. Significantly high r_2 relaxivity (860 mM^{-1} s^{-1}) and SAR (432 W/g) were reported by doping Zn^{2+} and Mn^{2+} simultaneously into 15 nm 2,3-dimercaptosuccinnic acid (DMSA) coated Fe_3O_4 nanoparticles.[11,12] In most cases, the diameter of the nanoparticles was very close to or above the superparamagnetic limit of MFe_2O_4 nanoparticles where there is always a possibility of magnetic aggregation that affects stability.

In addition to core nanoparticle, the selection of coating of MNS is equally critical. Any external materials without suitable coating get cleared from the blood circulation by the body's biological defense system that accumulate them in the liver and spleen. A diverse group of coatings such as dextran,[13] chitosan,[14] polyethylene glycol (PEG),[15] and silica[16] have been investigated to improve stability and biocompatibility in biological media. In particular, PEG coating has shown promise since it demonstrates excellent pharmacokinetic properties by inhibiting phagocytosis and prolonging blood circulation time of the MNS.[17] As a result, the PEG coating reduces nonspecific uptake in liver and spleen that promote active and/or passive targeting of MNS that has been one of the key issue in targeted theranostics.[18] There have been systematic studies with surface coating effect on r_2 relaxivity. Bao et al.[19] showed that the r_2 relaxivity of the DSPE-PEG coated 14 nm Fe_3O_4 nanoparticles first increased when the PEG molecular weight increased from 550 to 1000 and later decreased when the PEG size further increased to 2000 and 5000. The coatings are usually functionalized on the magnetic nanoparticle surface by an anchoring group. Amstad et al.[20] did a systematic study on such anchor groups that possess irreversible binding affinity to iron oxide nanoparticles. Nitrodopamine (NDOPA) showed the highest packing density and binding on the surface of iron oxide nanoparticles over other anchoring group including carboxylates and dopamine.

So far all the published reports are mainly focused on either theranostic properties (core + coating) or stability (coating + anchoring group) of MNS. What is missing is the system that has the both the qualities. Hence, the scope lies in the design of MNS that has optimized core nanoparticle composition and surface coating for improved stability and pharmacokinetics, and core nanoparticle size not close to superparamagnetic limit. Here we report MNS that has all qualities mentioned above and show significantly high theranostic potential. By engineering both the core composition and surface coating, the r_2 relaxivity up to 552 mM^{-1} s^{-1} and SAR up to 385 W/g were obtained. The size was chosen as 8 nm which is well below superparamagnetic limit and kept constant for all the nanoparticles to avoid any size effect on the theranostic properties. To the best of our knowledge, these are the highest values reported for MNS with core magnetic nanoparticles below 10 nm. MFe_2O_4 nanoparticles (where M = Fe, Mn, $Zn_{0.1}Mn_{0.9}$, $Zn_{0.2}Mn_{0.8}$, and $Zn_{0.4}Mn_{0.6}$) were synthesized as core of MNS to study the composition effect.

Considering the pharmacokinetics and stability, we designed a new ligand, nitrodopamine conjugated PEG (NDOPA-PEG) based on the findings by Amstad et al.[20] The surface coating effect was studied by tuning the PEG length of NDOPA-PEG functionalized MFe_2O_4 nanostructures. The free COOH group of NDOPA-PEG was utilized for conjugation of targeting agent and therapeutic cargo, as published elsewhere recently.[21] NDOPA-PEG coating on MFe_2O_4 nanostructures resulted in excellent colloidal stability in water, 150 mM PBS, 5 mM PB, and cell culture medium (SI Figure S1). The NDOPA-PEG coated MFe_2O_4 nanostructures showed biocompatibility when treated with Hela cells for Fe concentrations up to 200 μg/mL. Also, they showed reduced nonspecific uptake in macrophage cells in comparison to Ferumoxytol, a well known FDA approved contrast agent.

EXPERIMENTAL DETAILS

Synthesis of MFe_2O_4 Nanoparticles. The MFe_2O_4 nanoparticles were synthesized using well-known thermal decomposition method that resulted in monodispersity, single crystallinity, and controlled stoichiometric composition.[22] The precursors chosen were stable at ambient temperature that enables scaling of the process and magnetic nanoparticles in gram scale were obtained. The one-pot thermal decomposition approach was used to synthesize MFe_2O_4 nanoparticles (where M= Fe, Mn, Zn_xMn_{1-x}).[22] In a typical Fe_3O_4 nanoparticles synthesis, $Fe(acac)_3$ (2 mmol), 1,2-hexadecanediol (10 mmol), oleic acid (6 mmol), oleylamine (6 mmol), and benzyl ether (20 mL) were charged in a 100 mL three-neck round-bottom flask and magnetically stirred under a flow of nitrogen. The mixture was first heated to 110 °C for 1 h to remove moisture. Then the temperature was increased to 210 °C for 1 h and was finally refluxed for 1 h before cooling down to room temperature. The black-brown mixture was precipitated, washed three times using ethanol, and was then dispersed in hexane. The composition was changed by choosing different precursors and their ratios. $MnFe_2O_4$ nanoparticles were synthesized by adding $Fe(acac)_3$ (2 mmol) and $Mn(acac)_2$ (1 mmol) under identical conditions. Similarly, to synthesize $Zn_xMn_{1-x}Fe_2O_4$ nanoparticles, both $Zn(acac)_2$ (x mmol) and $Mn(acac)_2$ (1-x mmol) with $Fe(acac)_3$ (2 mmol) were used. The stoichiometry was controlled by tuning the initial molar ratio of the $Zn(acac)_2$ and $Mn(acac)_2$. Co^{2+} and Ni^{2+} were not used as dopants due to their toxicity and lower magnetic moment than Fe^{2+}, respectively.

Functionalization of MFe_2O_4 Nanoparticles. A novel ligand nitrodopamine functionalized PEG (NDOPA-PEG) was synthesized and functionalized on the MFe_2O_4 nanoparticles. The as-synthesized oleic acid coated hydrophobic MFe_2O_4 nanoparticles were functionalized with the NDOPA-PEG via ligand exchange process (Scheme 1).

Scheme 1. MFe_2O_4 Nanoparticles before and after Ligand Exchange[a]

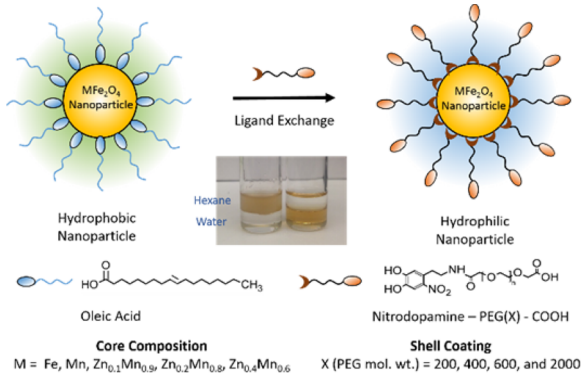

[a]The hydrophobic oleic acid coated MFe_2O_4 nanoparticles were made water-soluble after ligand exchange with nitrodopamine functionalized PEG (NDOPA-PEG).

DOI: 10.1021/acsami.6b01377
ACS Appl. Mater. Interfaces 2016, 8, 6953−6961

The length of PEG coating was tuned by changing the molecular weight of PEG. Nitrodopmine was synthesized from dopamine hydrochloride using previous reported method[23] and conjugated to one end of carboxylate functionalized PEG (biacid PEG) using EDC/NHS chemistry.[18] For conjugation, nitrodopamine (95 mg), PEG diacid (240 mg), *N*-hydroxysuccinimide (45 mg), *N*,*N*′-dicyclohexylcarbodiimide (80 mg), and sodium bicarbonate (200 mg) were dissolved in a mixture containing 20 mL chloroform and 40 mL dimethyl sulfoxide (DMSO). The solution was stirred at room temperature for 4 h for the reaction to be complete. MFe_2O_4 nanoparticles (25 mg) were then added and the resulting solution was sonicated overnight at room temperature under N_2 protection. The modified Fe_3O_4 nanoparticles were washed by dichloromethane 3 times, dried under nitrogen gas and were finally dispersed in water. The dispersion was dialyzed to remove any residual surfactants using a dialysis bag (MWCO = 10 000) for 2 days in water. A 200 nm syringe filter was used to remove any precipitation and the final concentration of the MFe_2O_4 nanostructures dispersed in water was determined by ICP-MS analysis. TEM showed that the particles did not aggregate after ligand exchange (SI Figure S4) and hydrodynamic sizes were found in the range of 22−47 nm, depending upon the length (mol. wt.) of the PEG coating. The NDOPA-PEG functionalized MFe_2O_4 nanostructures demonstrate high colloidal stability at a salt (NaCl) concentration of 150 mM, across a wide pH range (pH 6−10) and cell culture medium. Gel electrophoresis (1% agarose gel) was used to examine the stability in 150 mM PBS and 5 mM PB solution with DOPA-PEG and NDOPA-PEG (SI, Figure S1). The dark staining seen at the top of DOPA-PEG MNS lane indicates trapping of MNS at the top of the gel due to aggregation. However, no such staining was found in NDOPA-PEG MNS, showing the superiority of NDOPA coating over other coatings. The zeta-potential after functionalization was found to be in the range of −40 mV, consistent with their colloidal stability in water (SI, Figure S2). The atomic percent of Zn, Mn, and Fe was found to be very similar as initial precursor molar ratios as observed in EDX and ICP.

Structural and Magnetic Characterization. Particle size and distribution was observed on a Hitachi H8100 TEM (200 kV). The crystal structure of the particles was observed on Scintag powder XRD. The hydrodynamic diameters of the nanostructures was measured by Malvern Zeta Sizer Nano S-90 dynamic light scattering (DLS) instrument. TGA analysis was done by TA Instruments Q500 Thermogravimetric Analyzer. M-H hysteresis loops and FC/ZFC curves were recorded using superconducting quantum interference device (SQUID). Energy dispersive X-ray (EDX) of the nanostructures were observed at Hitachi HD2300 (SI, Figure S3).

Measurement of r_2 Relaxivity and Thermal Activation. MFe_2O_4 magnetic nanostructures dispersed in water were diluted to concentrations ranging from 0.01 to 0.11 mM of metal ion. T_2 relaxation times were determined at 3.0 T Magnetom Verio (Siemens Healthcare, Erlangen, Germany) using the multiple-echo-fast-spin−echo sequence. Multiple echo Spin echo sequence with TR = 1290 ms, 8 echo times starting with 9.9 to 79.2 ms, 160 mm FOV, 266 × 256 matrix, slice thickness 3 mm. Given that we had multiple samples with a distribution of T_2 relaxation times, we had to limit range of echo times. A commercial 12 channel head coil (diameter ∼160 mm) was used. A 1.5 mL eppendorf centrifuge tube was used as a sample holder. R_2 maps were generated using a custom software using Matlab. The signal decay was fit to a single exponential function to estimate T_2 on a pixel by pixel basis.

Thermal activation experiments were performed on an MSI Automation Inc. Hyperthermia Research System (model hyper 5) RF generator at a frequency of 300 kHz and a power of 5 kW. A 1 mL suspension (2 mg Fe/mL) was placed inside the 5 cm coil generating the AC magnetic field of 5 kA/m. A nonmagnetic nonmetallic optical temperature probe (Fiso) was used to monitor the temperature. Each experiment time duration was 10 min. A plot of time vs temperature was generated and used to calculate the specific absorption rate (SAR).

Cell Culture. HeLa human cervical cancer cell line was cultured in Dulbecco's modified Eagle's medium (DMEM) supplemented with 10% FBS and penicillin/streptomycin (100 units/mL and 100 μg/mL). J774 cells (kindly provided by Prof. Colby Shad Thaxton in the Department of Urology, Northwestern University Feinberg School of Medicine) were grown in RPMI-1640 medium containing 10% FBS and penicillin/streptomycin (100 units/mL and 100 μg/mL, respectively).

MTS Assay for Cell Viability Test. HeLa cells were plated at 10 000 cells per well in 96-well plate with 70−80% of confluency. MTS (3-(4,5-dimethylthiazol-2-yl)-5-(3-carboxymethoxyphenyl)-2-(4-sulfophenyl)-2H-tetrazolium) assay was used to quantify the cell viability according to the protocol provided by the manufacture (CellTiter 96 Aqueous One Solution Cell Proliferation Assay; Promega). Cell were incubated with different types of NDOPA-PEG_{600} coated nanostructures (Fe_3O_4, $MnFe_2O_4$, and $Z_{0.2}M_{0.8}Fe_2O_4$) at concentrations ranging from 1 to 200 μg/mL for 24 h at 37 °C Following treatment, cells were rinsed with PBS buffer briefly and further incubated with 20 μL of MTS stock solution into each well for additional 1−4 h at 37 °C. The optical densities were recorded at 490 nm and background absorbance at 700 nm was subtracted.

Quantitative Analysis of Cellular Uptake Pattern of MFe_2O_4 Nanostructures. For the quantitative analysis, J774 murine macrophage cells were seeded in 6-well cell culture plates (3×10^6 cells per well). Before the test, the cells were briefly washed with PBS twice and incubated with different types of MFe_2O_4 nanostructures (3 μg Fe/mL) for 1 h. Cells grown without any particles and with Ferumoxytol (commercially available contrast agent) were used as negative and positive control, respectively. After incubation, the membrane-bound particles were collected using the PBS-acetate buffer (20 mM sodium acetate in PBS, pH 3.0). All samples were digested with nitric acid and analyzed using ICP-MS.

RESULTS AND DISCUSSION

Figure 1a−d shows TEM images of MFe_2O_4 nanoparticles. It can be seen that all the particles are of same size (∼8 nm) and have a narrow size distribution. The excellent monodispersity of the MFe_2O_4 nanoparticles resulted in the large area assembly (Figure 1a). Figure 1a inset shows gram-scale quantity of the as-synthesized MFe_2O_4 nanoparticles. Structural information on MFe_2O_4 nanoparticles was obtained from both electron and X-ray diffraction. The stoichiometry was confirmed using EDX (SI, Figure S3). Figure 1e shows a selected area electron diffraction (SAED) pattern acquired from the 8 nm Fe_3O_4 nanoparticle assembly. The measured lattice spacing calculated from the rings in the diffraction pattern matches well with standard lattice spacing for bulk spinel phase of Fe_3O_4 with their respective *hkl* indexes (SI, Table S1). Figure 2 shows XRD patterns of as-synthesized Fe_3O_4, $MnFe_2O_4$, and $Zn_{0.2}Mn_{0.8}Fe_2O_4$ nanoparticles. The position and relative intensity of all diffraction peaks shows typical cubic spinel structure and matches well with standard Fe_3O_4 powder diffraction data (JCPDS 19−629). The size of the nanoparticles calculated using the Scherrer's formula[24] is consistent with the size determined by the statistical analysis of the TEM images (SI, Table S2), indicating each nanoparticle is a single crystal. Figure 2 inset shows enlarged view of the main peak (311) of Fe_3O_4, $MnFe_2O_4$, and $Zn_{0.2}Mn_{0.8}Fe_2O_4$ nanoparticles. The peak position for $MnFe_2O_4$ and $Zn_{0.2}Mn_{0.8}Fe_2O_4$ nanoparticles shifted to a lower diffraction angle due to lattice strain, confirming the successful incorporation of Mn^{2+} and Zn^{2+} ions in the Fe_3O_4 nanoparticles.

Figure 3a shows the M-H loops of as-synthesized MFe_2O_4 nanoparticles measured at room temperature. The particles show no hysteresis and demonstrate superparamagnetic behavior at room temperature which is ideal for their use in biomedical applications. For Fe_3O_4 nanoparticles, saturation magnetization (M_s) was found to be 45 emu/g of metal ions. This value was increased with Mn^{2+} doping and the M_s of

DOI: 10.1021/acsami.6b01377
ACS Appl. Mater. Interfaces 2016, 8, 6953−6961

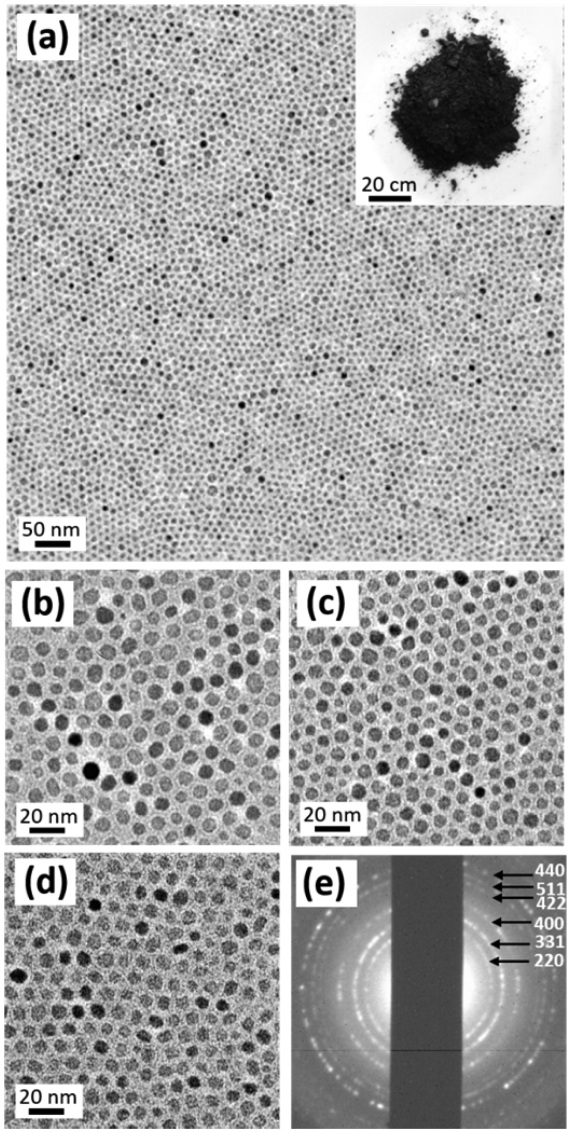

Figure 1. TEM images of (a,b) Fe_3O_4, (c) $MnFe_2O_4$, and (d) $Zn_{0.2}Mn_{0.8}Fe_2O_4$ nanoparticles. All the nanoparticles were monodisperse and of size ~8 nm. (e) Electron diffraction pattern of Fe_3O_4 nanoparticles. The inset in panel (a) shows 1.3 g of as-synthesized MFe_2O_4 nanoparticles.

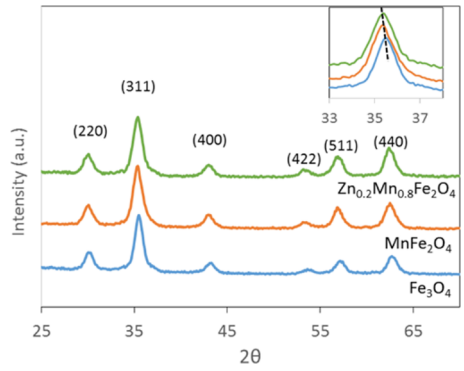

Figure 2. XRD spectra of as-synthesized Fe_3O_4, $MnFe_2O_4$, and $Zn_{0.2}Mn_{0.8}Fe_2O_4$ nanoparticles. All the spectra show inverse spinal AB_2O_4 structure. The grain size calculated from fwhm of (311) peak using Scherrer's formula matches well the particle size obtained from TEM. Inset figure shows main XRD characteristic peak (311) of Fe_3O_4, $MnFe_2O_4$, and $Zn_{0.2}Mn_{0.8}Fe_2O_4$ nanoparticles. The peak positions of $MnFe_2O_4$ and $Zn_{0.2}Mn_{0.8}Fe_2O_4$ shift due to lattice strain which is a clear indicator of Mn and Zn doping into Fe_3O_4 nanoparticles.

$MnFe_2O_4$ nanoparticles was observed up to 84 emu/g of metal ions. This increase can be explained by arrangement of Fe^{2+}, Fe^{3+}, and Mn^{2+} ions in the crystal lattice of $MnFe_2O_4$ nanoparticles. Fe_3O_4 nanoparticles have an inverse spinel crystal structure composed of face-centered cubic lattice of oxygen atoms. The octahedral sites (O_h) of the lattice is occupied by Fe^{3+} and Fe^{2+} ions whereas the tetrahedral sites (T_d) are occupied by Fe^{3+} ions (Figure 3b). The magnetic spins of Fe^{3+} ions at the O_h and T_d sites align opposite to each other and hence cancel. Therefore, the net magnetization of Fe_3O_4 nanoparticle is decided by magnetic moment of Fe^{2+} ions (4 μ_B) located on O_h sites. In case of $MnFe_2O_4$ nanoparticles, the Mn^{2+} ions replaces Fe^{2+} ions on O_h sites. Hence, the higher magnetic moment of Mn^{2+} (5 μ_B) results in higher saturation magnetization of $MnFe_2O_4$ nanoparticles than Fe_3O_4 nanoparticles.

Interestingly, simultaneous doping of Mn^{2+} and Zn^{2+} ions in Fe_3O_4 nanoparticles further increased the saturation magnetization up to 110 emu/g of metal ions though Zn^{2+} ions have no magnetic moment. Since $ZnFe_2O_4$ has a normal spinel structure, Zn^{2+} ions prefers to occupy T_d sites. As a result, spins of Fe^{3+} at O_h and T_d sites do not cancel each other completely and the net magnetic moment increases due to the contribution of Mn^{2+} as well Fe^{3+} ions (Figure 3b). The magnetization of $(Zn_xMn_{1-x})Fe_2O_4$ nanoparticles initially increases with doping of Zn^{2+} ions (95 and 110 emu/g of metal ions for x = 0.1 and 0.2, respectively). However, at higher Zn^{2+} ions doping levels, Fe^{3+} ions at O_h sites starts increasing and the antiferromagnetic interaction of Fe^{3+} ions at O_h sites starts dominating, resulting in the drop of the net magnetic moment (89 emu/g of metal ions for x = 0.4). The similar trend has also been shown by Cheon et al.[11] This is the reason why the theoretical value of M_s for $ZnFe_2O_4$ (x = 1) is predicted as zero since all the Zn^{2+} ions occupy T_d sites while all Fe^{3+} ions occupy O_h sites. The antiferromagnetic interactions between Fe^{3+} ions dominate, cancel each other's moment and net moment becomes zero.[25] Based on the magnetization values, $Zn_{0.2}Mn_{0.8}Fe_2O_4$ nanoparticles were chosen for r_2 relaxivity and thermal activation measurements for comparison with Fe_3O_4 and $MnFe_2O_4$ nanoparticles.

Though all the MFe_2O_4 nanoparticles showed superparamagnetic behavior at room temperature, the M-H loops measured at 4K showed ferromagnetic nature, indicating their blocking temperature (T_b) between 4K and room temperature. To find out the T_b, field-cooling (FC) and zero-field-cooling (ZFC) magnetization plots were measured at 100 Oe (Figure 3c). The T_b of Fe_3O_4 (blue), $MnFe_2O_4$ (orange), and $Zn_{0.2}Mn_{0.8}Fe_2O_4$ (green) nanoparticles was observed as 35, 75, and 100 K, respectively, suggesting the T_b increases after doping of Fe_3O_4 nanoparticles. It is well-known the T_b is strongly dependent on the size of the nanoparticles.[26] However, in this case since the particle size of all MFe_2O_4 nanoparticles are similar, the highest T_b could be correlated to the strongest coupling strength between electron spin and orbital angular momentum (L-S).[27] In other words, $Zn_{0.2}Mn_{0.8}Fe_2O_4$ nanoparticles showed highest anisotropy among all. Other than shift, broadening of the ZFC peak was also observed in the doped samples. Often, the broadening has been correlated with the

DOI: 10.1021/acsami.6b01377
ACS Appl. Mater. Interfaces 2016, 8, 6953−6961

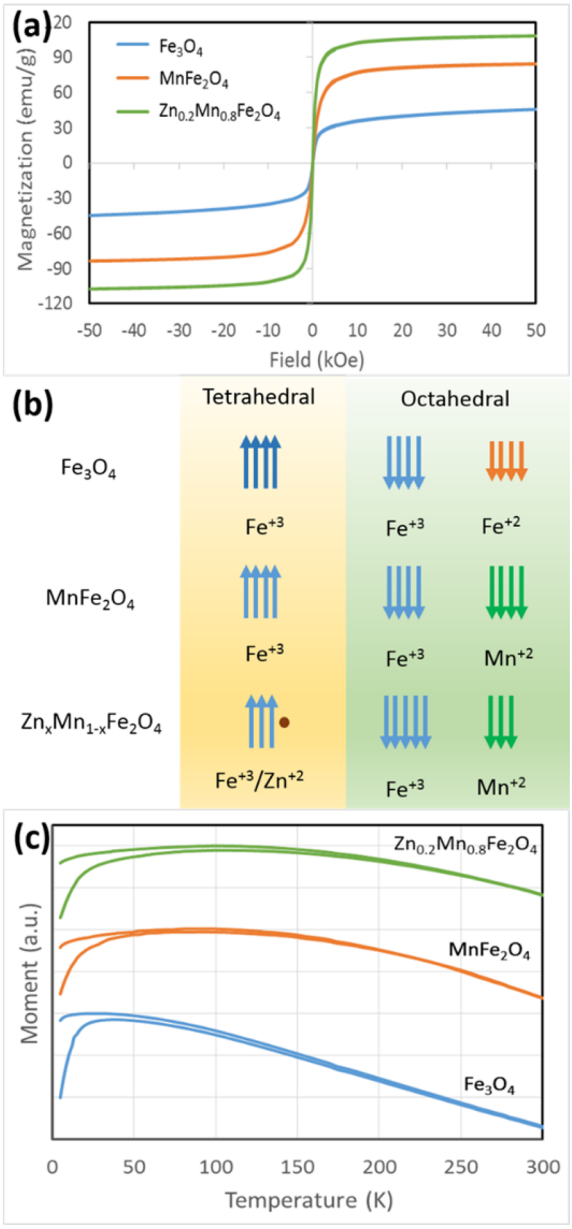

Figure 3. (a) Room temperature M-H hysteresis loops, (b) position of Fe^{3+}, Fe^{2+}, Zn^{2+}, and Mn^{2+} ions in crystal lattice, and (c) FC-ZFC curves of as-synthesized Fe_3O_4 (blue), $MnFe_2O_4$ (orange), and $Zn_{0.2}Mn_{0.8}Fe_2O_4$ (green) nanoparticles. The hysteresis loops shows all the nanoparticles are superparamagnetic and the highest saturation magnetization of 103 emu/g was observed with $Zn_{0.2}Mn_{0.8}Fe_2O_4$ nanoparticles, double than saturation magnetization of 51 emu/g of Fe_3O_4 nanoparticles. The FC-ZFC curve of Fe_3O_4 shows the blocking temperature increased from ~40 to 110 K after doping with $(Zn_xMn_{1-x})^{+2}$, suggesting highest anisotropy in $Zn_{0.2}Mn_{0.8}Fe_2O_4$ nanoparticles.

large size distribution of nanoparticles.[28] However, since the size distribution of the nanoparticles is very narrow in our case, the broadening can be explained due to the increased interparticle interactions that arise from either dipolar interactions between nanoparticles or the exchange interactions between the magnetic ions at the surface of nanoparticles.[29] The surfactant coating on nanoparticle increases the spacing between particles that results in negligible exchange interactions. Hence, the dipolar interactions are the main source of the interparticle interaction.[30,31] The dipole interaction energy of a nanoparticle is calculated as[32]

$$E_d = \frac{\mu_0}{4\pi}\frac{M^2}{d^3} \quad (1)$$

where M is the magnetic moment and d is interparticle distance. Since the interparticle distance is same for all MFe_2O_4 nanoparticles (due to the same coating), the difference in their magnetic moment could be attributed to increased dipolar interaction.[33,34] It is clear from the Figure 3b that $Zn_{0.2}Mn_{0.8}Fe_2O_4$ with highest dipolar interaction results in most broadened ZFC peak.

In magnetic resonance imaging (MRI), the T_2 contrast enhancement effect of MNS is measured by r_2 relaxivity, a slope of relaxation rate R_2 (s^{-1}) plotted against MNS metal concentration (mM). The higher relaxivity corresponds to higher T_2 contrast enhancement effect. The r_2 relaxation rate of MNS is defined as

$$R_2 = \frac{1}{T_2} = \frac{256\pi^2\gamma^2}{405}M_s^2 V\frac{r^2}{D\left(1+\frac{L}{r}\right)} \quad (2)$$

where T_2 is transverse relaxation time, γ is proton gyromagnetic ratio, M_s is saturation magnetization, V is volume of MNS, D is diffusion coefficient of water molecules, r is radius of MNS core, and L is thickness of MNS surface coating.[35] According to the eq 2, the increased magnetization values of $Zn_xMn_{1-x}Fe_2O_4$ MNS should enhance T_2 contrast in MR imaging compare to Fe_3O_4 MNS. Figure 4 shows r_2 relaxivity plots and color coded T_2-weighted magnetic resonance (MR) images of NDOPA-PEG_{600} coated MFe_2O_4 nanostructures coated along with Ferumoxtran and Ferumoxide (dextran coated Fe_3O_4 nanoparticles). The spin−spin relaxation time (T_2) was observed at 3 T. Consistent with the magnetization results, $Zn_{0.2}Mn_{0.8}Fe_2O_4$ nanostructures showed the strongest MR

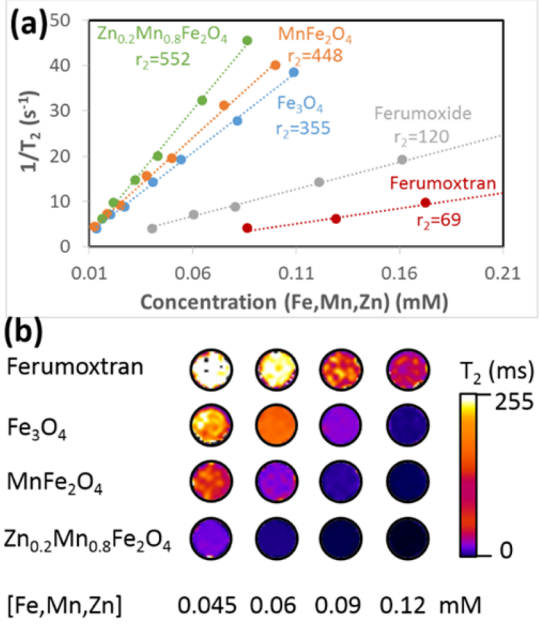

Figure 4. (a) r_2 relaxivity plots and (b) color coded T_2-weighted (3 T) magnetic resonance (MR) images of NDOPA-PEG coated Fe_3O_4, $MnFe_2O_4$, and $Zn_{0.2}Mn_{0.8}Fe_2O_4$ nanostructures along with Ferumoxtran and Ferumoxide (dextran coated Fe_3O_4 nanoparticles).

DOI: 10.1021/acsami.6b01377
ACS Appl. Mater. Interfaces 2016, 8, 6953−6961

contrast effect with the r_2 relaxivity of 552 mM^{-1} s^{-1} while the $MnFe_2O_4$ and Fe_3O_4 nanostructures demonstrated r_2 relaxivity of 448 and 355 mM^{-1} s^{-1}. The increase in the r_2 relaxivity from 355 to 552 mM^{-1} s^{-1} by just tuning the core composition shows that the composition of the MNS core is critical for modulating the spin−spin relaxation processes of protons in the water molecules surrounding the MNS. It should also be noted that the highest r_2 relaxivity obtained from our PEG coated sample is ∼8 times higher than Ferumoxtran (dextran coated iron oxide nanoparticles), a well-known iron oxide MNS based MRI contrast agent. One possibility of higher r_2 relaxivity is due to clustering of MNS during ligand exchange. Just to confirm that, TEM was observed after NDOPA-PEG coating (SI Figure S4). No aggregation of MNS was observed confirming that higher relaxivity was due to doping and not clustering of MNS.

MNS can be thermally activated and generate heat under an external RF field that makes the MNS unique for noninvasive therapeutic applications in biomedicine.[36] Rosensweig et al.[37] described the analytical relationships and computational models of thermal activation in a suspension of magnetic nanoparticles under an external RF field. Thermal activation of the MNS under an external RF field is defined as specific absorption rate (SAR) that is the amount of heat generated per unit gram of the MNS. Higher SAR is critical in order to obtain high therapeutic efficacy of MNS in biomedical applications. The SAR for monodisperse magnetic nanostructures under an external RF field can be calculated as

$$\mathrm{SAR} = \frac{\mu_0 \chi_0 {H_0}^2}{2\rho\varphi} 2\pi f \frac{2\pi f\tau}{1 + (2\pi f\tau)^2} \tag{3}$$

where μ_0 is the permeability of free space, H_0 is the magnetic field intensity in the material, and f is the field frequency. χ_0 is the equilibrium susceptibility and can be calculated as

$$\chi_0 = \frac{(\mu_0 {m_s}^2 \varphi V)}{kT} \frac{\coth\left(\xi - \frac{1}{\xi}\right)}{\xi} \tag{4}$$

where m_s is saturation magnetization of magnetic nanoparticle, V is sample volume, ξ is Langevin parameter, φ is volume fraction of magnetic nanostructures, k is Boltzmann constant, and T is the temperature.

Figure 5 shows the thermal activation plots and SAR values of NDOPA-PEG_{600} coated Fe_3O_4, $MnFe_2O_4$, and $Zn_{0.2}Mn_{0.8}Fe_2O_4$ nanostructures ([Fe+Mn+Zn] = 2 mg/mL) under RF field of 5 kA/m (5 kW, 300 kHz). The field (H_0) and frequency (f) were chosen such that the $H_0 f$ factor was well below the experimentally estimated threshold of 5×10^9 A/ms.[38] SAR was calculated from the thermal activation plots using the following equation

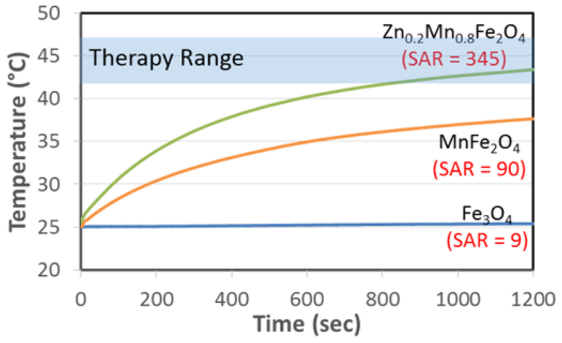

Figure 5. Thermal activation plots and SAR values of NDOPA-PEG_{600} coated Fe_3O_4, $MnFe_2O_4$, and $Zn_{0.2}Mn_{0.8}Fe_2O_4$ (green) nanostructures. The thermal activation plots shows drastic change in dT/dt in three different ferrites that resulted in significant difference in their SAR values.

$$\mathrm{SAR} = \frac{CV_s}{m}\left(\frac{dT}{dt}\right) \tag{5}$$

where C is the specific heat capacity of the solvent, dT/dt is the initial slope of the thermal activation plot, Vs is the sample volume, and m is mass of magnetic material in the sample. According to the eqs 3 and 4, the SAR is highly dependent on the saturation magnetization of the MNS. The calculated SAR values based on the thermal activation plots showed that NDOPA-PEG_{600} coated $Zn_{0.2}Mn_{0.8}Fe_2O_4$ nanostructures with a higher magnetization and anisotropy have superior thermal activation properties over NDOPA-PEG_{600} coated $MnFe_2O_4$ and Fe_3O_4 nanostructures. The SAR value of 8 nm $Zn_{0.2}Mn_{0.8}Fe_2O_4$ nanostructures is 345 W/g, four times higher than 8 nm $MnFe_2O_4$ (90 W/g) and around 40 times higher than 8 nm Fe_3O_4 nanostructures (9 W/g). This dramatic change in SAR further support our claim that tuning composition can significantly enhance theranostic properties of MNS.

The surface coating effect was studied by tuning the PEG length of NDOPA-PEG coating. $Zn_{0.2}Mn_{0.8}Fe_2O_4$ nanostructures (size 8 nm) were used as core selected for the study due to their higher theranostic properties among all MFe_2O_4 nanostructures. The measured hydrodynamic diameters of the NDOPA-PEG coated $Zn_{0.2}Mn_{0.8}Fe_2O_4$ nanostructures with PEG mol. wt. 200, 400, 600, and 2000 were observed to be 22, 25, 34, and 47 nm, confirming that larger mol. wt. of PEG resulted in longer length extended away from the nanoparticle surface. The r_2 relaxivity of the $Zn_{0.2}Mn_{0.8}Fe_2O_4$ nanostructures increased when the PEG chain length increased from 200 to 600 (Figure 6a). The significantly higher relaxivity of all the NDOPA-PEG coated MNS over widely used dextran and silica coated MNS suggest that water permeable PEG layer influence the spin−spin relaxation processes of water protons in a much larger area than dextran and silica. According to eq 1, the r_2 relaxivity is inversely proportional to the coating thickness and r_2 should decrease with increasing coating thickness. However, the eq 2 assumes the coating (L) as impermeable[39] but the PEG coating is permeable to water, hence the inversely proportional relationship cannot be correlated with our results. Since protons that are within the range of PEG coating will relax much faster than those in bulk water, it is expected observe increment in r_2 values with increasing PEG thickness. However, with further increasing the PEG coating length to 2000 reduced the r_2 values (Figure 6a). These results clearly indicate that an optimum PEG coating is required to obtain the highest r_2 relaxivity. The similar trend was demonstrated by Bao et al.[19,40] They showed that the r_2 relaxivity of the DSPE-PEG coated 14 nm Fe_3O_4 nanostructures first increased when the PEG molecular weight increased from 550 to 1000 and later decreased when the PEG size further increased to 2000 and 5000. They addressed this issue experimentally as well as theoretically by developing two simulation models. They explained there are several competing factors such as thickness and packing of hydrophilic and hydrophobic parts of the polymer determine the final r_2 of a magnetic nanostructure.

DOI: 10.1021/acsami.6b01377
ACS Appl. Mater. Interfaces 2016, 8, 6953−6961

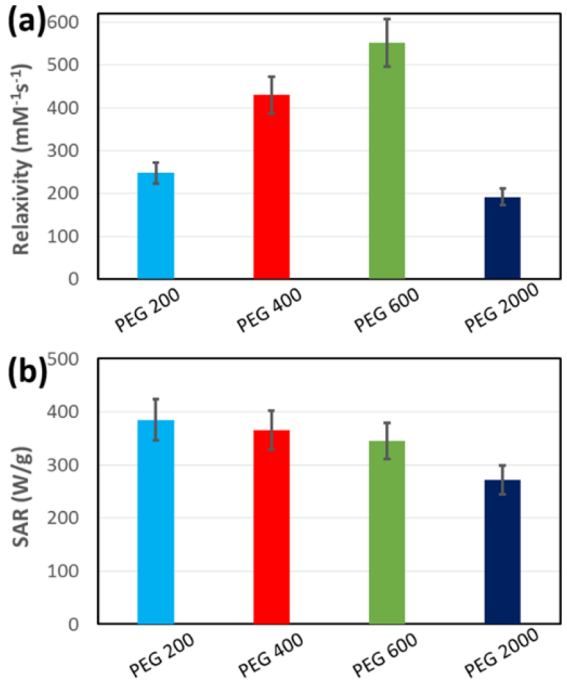

Figure 6. (a) r_2 relaxivity values and (b) specific absorption rates of NDOPA-PEG coated $Zn_{0.2}Mn_{0.8}Fe_2O_4$ nanostructures with variable PEG chain length (PEG mol. wt. 200, 400, 600, and 2000).

On the other hand, the SAR of $Zn_{0.2}Mn_{0.8}Fe_2O_4$ nanostructures decreased when the PEG chain length increased from 200 to 2000 (Figure 6b). The surface coating affects the Brownian relaxation of MNS which is based on a physical rotation of MNS and one of the main reason for thermal activation of MNS. Hence, thicker coating can result in higher Brownian losses that reduces the SAR of MNS which is consistent with our observations. So, there is certainly a trade-off between r_2 and SAR with increasing PEG thickness. However, the drop in SAR was not as significant as increment in r_2 with increasing PEG thickness. Hence we chose NDOPA-PEG_{600} to do further in vitro studies.

The cytotoxicity of NDOPA-PEG_{600} coated MFe_2O_4 MNS was evaluated using an MTS assay on HeLa cells. It is a colorimetric assay that determines the quantity of formazan end product, which is directly proportional to the number of viable cells. The ratio of absorbance in treatment wells to control was used to report percent viability of HeLa cells. It is evident from the Figure 7 that even at concentrations as high as 200 μg/mL of NDOPA-PEG coated MFe_2O_4 MNS, the viability of HeLa cells was not affected significantly. This indicates that the particles at the concentrations reported here, do not induce toxic effects in the cells making them biocompatible for further use as theranostic agents.

To check whether PEG coating reduce nonspecific uptake by macrophages, we have investigated the cellular uptake pattern of NDOPA-PEG coated MFe_2O_4 nanostructures incubated with J774 macrophage cell line at the concentration of 3 μg Fe/mL for 1 h at 37 °C. The concentration of Fe ion bound to membrane were measured by using inductively coupled plasma - mass spectrometry (ICP-MS) analysis. The samples treated with Ferumoxytol (polyglucose sorbitol coated Fe_3O_4 nanostructures) with same Fe concentration were used as a control for comparison. NDOPA-PEG coated MFe_2O_4 nanostructures showed ~51 to 70% lower Fe ion uptake than Ferumoxytol

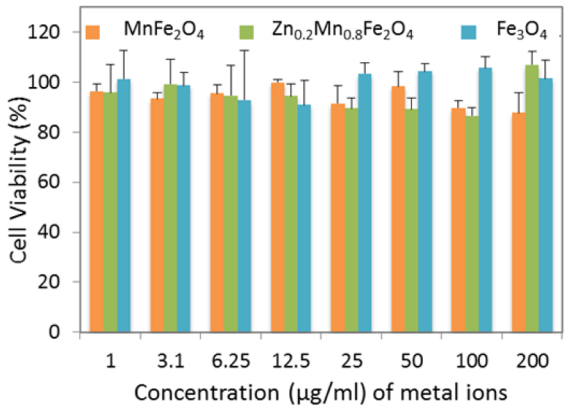

Figure 7. Cell viability of HeLa cells after treatment with NDOPA-PEG_{600} coated Fe_3O_4 (blue), $MnFe_2O_4$ (orange), and $Zn_{0.2}Mn_{0.8}Fe_2O_4$ (green) MNS at concentrations ranging from 1 to 200 μg/mL of metal ions for 24 h. MTS reading with untreated cells was used as a control.

(Figure 8), confirming that our NDOPA-PEG coated MNS show reduced nonspecific uptake in macrophage cells that can

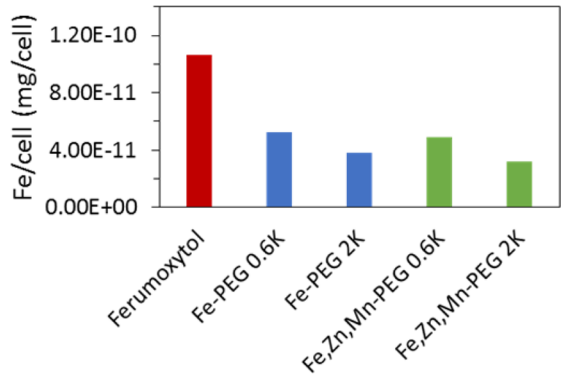

Figure 8. Macrophage uptake study of NOPDA-PEG coated MFe_2O_4 nanostructures in J774 macrophage cells after 1 h incubation with 3 μg Fe/mL. Fe uptake in the membrane-bound portion in cells shows that Ferumoxytol shows the highest uptake and the uptake drops ~51 to 70% for NDOPA-PEG coated MFe_2O_4 nanostructures.

result in longer blood circulation time. Further, we noticed that Fe ion uptake decreased with increasing PEG length of nanostructures, indicating that length of PEG chain also affect the nonspecific uptake by macrophage cells.

SUMMARY AND CONCLUSIONS

We have developed a facile and scalable approach to synthesize MNS with MFe_2O_4 (M= Fe, Mn, Zn_xMn_{1-x}) nanoparticles as core and nitrodopamine conjugated PEG (NDOPA-PEG) as surface coating. By tuning the core composition and length of surface coating, enhanced theranostic properties of magnetic nanostructures were obtained, indicating that both core as well as coating are important factors to take into consideration during the design of theranostic MNS. The composition was controlled by doping Mn^{2+} and Zn^{2+} ions into Fe_3O_4 nanoparticles and tuning their stoichiometry while the length of surface coating was tuned by changing the mol. wt. of PEG. These engineered magnetic nanostructures with enhanced magnetization and anisotropy (M_s = 110 emu/g and T_B = 100 K) resulted in r_2 relaxivity value up to 552 mM^{-1} s^{-1} (3 T) and SAR up to 385 W/g (5kA/m, 5 kW, 300 kHz) which are

DOI: 10.1021/acsami.6b01377
ACS Appl. Mater. Interfaces 2016, 8, 6953−6961

among the highest values reported for MNS with similar size core magnetic nanoparticles (<10 nm). By increasing the particle size, the r_2 relaxivity and SAR of our particles can be further increased. However, intention to choose 8 nm core size was to stay well below superparamagnetic limit and avoid any possibility of aggregation. In addition, NDOPA-PEG coated MFe_2O_4 nanostructures showed enhanced biocompatibility (up to [Fe] = 200 μg/mL) and reduced nonspecific uptake in macrophage cells in comparison to other well established FDA approved Fe based MR contrast agents. When coupled with the desired targeting agents, these ultrastable MNS have great potential in targeted theranostic applications.

■ ASSOCIATED CONTENT

Supporting Information

The Supporting Information is available free of charge on the ACS Publications website at DOI: 10.1021/acsami.6b01377.

Measured lattice spacing based on the rings in SAED pattern of Fe_3O_4 nanoparticles, size of the MFe_2O_4 nanoparticles calculated using the Scherrer's formula, stability test of Fe_3O_4 MNS in a 1% agarose gel, zeta potential of MFe_2O_4 nanostructures and EDX of a single $Zn_{0.2}Mn_{0.8}Fe_2O_4$ nanoparticle. (PDF)

■ AUTHOR INFORMATION

Corresponding Author

*E-mail: v-dravid@northwestern.edu. Phone: +1-847-467-1363. Fax: +1-847-467-6573.

Notes

The authors declare no competing financial interest.

■ ACKNOWLEDGMENTS

The authors would like to thank Prof. M. Aslam (IIT Bombay, India) for the intellectual discussion. This research was supported by the Center of Cancer Nanotechnology Excellence (CCNE) initiative of the National Institutes of Health (NIH) under Award number U54 CA151880. Any opinions, findings, conclusions, or recommendations expressed in this material are those of the authors and do not necessarily reflect those of the NIH. V.N., S.K., S.R., and V.P.D. gratefully acknowledges support from the NTU-NU Institute for NanoMedicine located at the International Institute for Nanotechnology, Northwestern University, USA and the Nanyang Technological University, Singapore. This work made use of the (EPIC, Keck-II, and/or SPID) facility(ies) of the NUANCE Center at Northwestern University, which has received support from the Soft and Hybrid Nanotechnology Experimental (SHyNE) Resource (NSF NNCI-1542205); the MRSEC program (NSF DMR-1121262) at the Materials Research Center; the International Institute for Nanotechnology (IIN); the Keck Foundation; and the State of Illinois, through the IIN.

■ REFERENCES

(1) Moghimi, S. M.; Hunter, A. C.; Murray, J. C. Nanomedicine: Current Status and Future Prospects. *FASEB J.* **2005**, *19*, 311−330.

(2) Sun, C.; Lee, J. S. H.; Zhang, M. Q. Magnetic Nanoparticles in MR Imaging and Drug Delivery. *Adv. Drug Delivery Rev.* **2008**, *60*, 1252−1265.

(3) De, M.; Chou, S. S.; Joshi, H. M.; Dravid, V. P. Hybrid Magnetic Nanostructures (MNS) for Magnetic Resonance Imaging Applications. *Adv. Drug Delivery Rev.* **2011**, *63*, 1282−1299.

(4) Lee, N.; Hyeon, T. Designed Synthesis of Uniformly Sized Iron Oxide Nanoparticles for Efficient Magnetic Resonance Imaging Contrast Agents. *Chem. Soc. Rev.* **2012**, *41*, 2575−2589.

(5) Yoo, D.; Lee, J. H.; Shin, T. H.; Cheon, J. Theranostic Magnetic Nanoparticles. *Acc. Chem. Res.* **2011**, *44*, 863−874.

(6) Nandwana, V.; De, M.; Chu, S.; Jaiswal, M.; Rotz, M.; Meade, T. J.; Dravid, V. P. Nanotechnology-Based Precision Tools for the Detection and Treatment of Cancer. In *Cancer Treat. Res.*; Mirkin, C. A., Meade, T. J., Hurst Petrosko, S., Stegh, A. H., Eds.; 2015; Chapter Theranostic Magnetic Nanostructures (MNS) for Cancer, Vol. *166*, pp 51−83.10.1007/978-3-319-16555-4_3

(7) Reddy, L. H.; Arias, J. L.; Nicolas, J.; Couvreur, P. Magnetic Nanoparticles: Design and Characterization, Toxicity and Biocompatibility, Pharmaceutical and Biomedical Applications. *Chem. Rev.* **2012**, *112*, 5818−5878.

(8) Jun, Y. W.; Huh, Y. M.; Choi, J. S.; Lee, J. H.; Song, H. T.; Kim, S.; Yoon, S.; Kim, K. S.; Shin, J. S.; Suh, J. S.; Cheon, J. Nanoscale Size Effect of Magnetic Nanocrystals and Their Utilization for Cancer Diagnosis Via Magnetic Resonance Imaging. *J. Am. Chem. Soc.* **2005**, *127*, 5732−5733.

(9) Lee, N.; Kim, H.; Choi, S. H.; Park, M.; Kim, D.; Kim, H. C.; Choi, Y.; Lin, S.; Kim, B. H.; Jung, H. S.; Kim, H.; Park, K. S.; Moon, W. K.; Hyeon, T. Magnetosome-Like Ferrimagnetic Iron Oxide Nanocubes for Highly Sensitive Mri of Single Cells and Transplanted Pancreatic Islets. *Proc. Natl. Acad. Sci. U. S. A.* **2011**, *108*, 2662−2667.

(10) de la Presa, P.; Luengo, Y.; Multigner, M.; Costo, R.; Morales, M. P.; Rivero, G.; Hernando, A. Study of Heating Efficiency as a Function of Concentration, Size, and Applied Field in Gamma-Fe2o3 Nanoparticles. *J. Phys. Chem. C* **2012**, *116*, 25602−25610.

(11) Jang, J. T.; Nah, H.; Lee, J. H.; Moon, S. H.; Kim, M. G.; Cheon, J. Critical Enhancements of Mri Contrast and Hyperthermic Effects by Dopant-Controlled Magnetic Nanoparticles. *Angew. Chem., Int. Ed.* **2009**, *48*, 1234−1238.

(12) Barcena, C.; Sra, A. K.; Chaubey, G. S.; Khemtong, C.; Liu, J. P.; Gao, J. Zinc Ferrite Nanoparticles as MRI Contrast Agents. *Chem. Commun.* **2008**, 2224−2226.

(13) Mornet, S.; Portier, J.; Duguet, E. A Method for Synthesis and Functionalization of Ultrasmall Superparamagnetic Covalent Carriers Based on Maghemite and Dextran. *J. Magn. Magn. Mater.* **2005**, *293*, 127−134.

(14) Kim, D. H.; Kim, K. N.; Kim, K. M.; Lee, Y. K. Targeting to Carcinoma Cells with Chitosan- and Starch-Coated Magnetic Nanoparticles for Magnetic Hyperthermia. *J. Biomed. Mater. Res., Part A* **2009**, *88A*, 1−11.

(15) Kohler, N.; Fryxell, G. E.; Zhang, M. Q. A Bifunctional Poly(Ethylene Glycol) Silane Immobilized on Metallic Oxide-Based Nanoparticles for Conjugation with Cell Targeting Agents. *J. Am. Chem. Soc.* **2004**, *126*, 7206−7211.

(16) Ma, D. L.; Veres, T.; Clim, L.; Normandin, F.; Guan, J. W.; Kingston, D.; Simard, B. Superparamagnetic Fe(X)Oy@Sio2 Core-Shell Nanostructures: Controlled Synthesis and Magnetic Characterization. *J. Phys. Chem. C* **2007**, *111*, 1999−2007.

(17) Harris, J. M.; Chess, R. B. Effect of Pegylation on Pharmaceuticals. *Nat. Rev. Drug Discovery* **2003**, *2*, 214−221.

(18) Xie, J.; Xu, C.; Kohler, N.; Hou, Y.; Sun, S. Controlled Pegylation of Monodisperse Fe3O4 Nanoparticles for Reduced Non-Specific Uptake by Macrophage Cells. *Adv. Mater.* **2007**, *19*, 3163−3166.

(19) Tong, S.; Hou, S. J.; Zheng, Z. L.; Zhou, J.; Bao, G. Coating Optimization of Superparamagnetic Iron Oxide Nanoparticles for High T-2 Relaxivity. *Nano Lett.* **2010**, *10*, 4607−4613.

(20) Amstad, E.; Gillich, T.; Bilecka, I.; Textor, M.; Reimhult, E. Ultrastable Iron Oxide Nanoparticle Colloidal Suspensions Using Dispersants with Catechol-Derived Anchor Groups. *Nano Lett.* **2009**, *9*, 4042−4048.

(21) Viola, K. L.; Sbarboro, J.; Sureka, R.; De, M.; Bicca, M. A.; Wang, J.; Vasavada, S.; Satpathy, S.; Wu, S.; Joshi, H.; Velasco, P. T.; MacRenaris, K.; Waters, E. A.; Lu, C.; Phan, J.; Lacor, P.; Prasad, P.;

DOI: 10.1021/acsami.6b01377
ACS Appl. Mater. Interfaces 2016, 8, 6953−6961

Dravid, V. P.; Klein, W. L. Towards Non-Invasive Diagnostic Imaging of Early-Stage Alzheimer's Disease. *Nat. Nanotechnol.* **2015**, *10*, 91−98.
(22) Sun, S. H.; Zeng, H.; Robinson, D. B.; Raoux, S.; Rice, P. M.; Wang, S. X.; Li, G. X. Monodisperse MFe2O4 (M = Fe, Co, Mn) Nanoparticles. *J. Am. Chem. Soc.* **2004**, *126*, 273−279.
(23) Napolitano, A.; Dischia, M.; Costantini, C.; Prota, G. A New Oxidation Pathway of the Neurotoxin 6-Aminodopamine - Isolation and Characterization of a Dimer with a Tetrahydro[3,4a]-Iminoethanophenoxazine Ring-System. *Tetrahedron* **1992**, *48*, 8515−8522.
(24) Cullity, B. D. *Elements of X-Ray Diffraction*; Addison-Wesley Pub. Co.: Reading, Mass., 1956; p 514.
(25) Schiessl, W.; Potzel, W.; Karzel, H.; Steiner, M.; Kalvius, G. M.; Martin, A.; Krause, M. K.; I, H.; Gal, J.; Schafer, W.; Will, G.; Hillberg, M.; Wappling, R. Magnetic Properties of the Znfe2o4 Spinel. *Phys. Rev. B: Condens. Matter Mater. Phys.* **1996**, *53*, 9143−9152.
(26) Park, J.; An, K. J.; Hwang, Y. S.; Park, J. G.; Noh, H. J.; Kim, J. Y.; Park, J. H.; Hwang, N. M.; Hyeon, T. Ultra-Large-Scale Syntheses of Monodisperse Nanocrystals. *Nat. Mater.* **2004**, *3*, 891−895.
(27) Song, Q.; Zhang, Z. J. Correlation between Spin-Orbital Coupling and the Superparamagnetic Properties in Magnetite and Cobalt Ferrite Spinel Nanocrystals. *J. Phys. Chem. B* **2006**, *110*, 11205−11209.
(28) Shiratsuchi, Y.; Yamamoto, M. Dominant Factor of Zero-Field-Cooled Magnetization in Discontinuous Fe Films. *Phys. Rev. B: Condens. Matter Mater. Phys.* **2007**, *76*.10.1103/PhysRevB.76.144432
(29) Morup, S.; Hansen, M. F.; Frandsen, C. Magnetic Interactions between Nanoparticles. *Beilstein J. Nanotechnol.* **2010**, *1*, 182−190.
(30) Held, G. A.; Grinstein, G.; Doyle, H.; Sun, S. H.; Murray, C. B. Competing Interactions in Dispersions of Superparamagnetic Nanoparticles. *Phys. Rev. B: Condens. Matter Mater. Phys.* **2001**, *64*.10.1103/PhysRevB.64.012408
(31) Vestal, C. R.; Song, Q.; Zhang, Z. J. Effects of Interparticle Interactions Upon the Magnetic Properties of CoFe2O4 and MnFe2O4 Nanocrystals. *J. Phys. Chem. B* **2004**, *108*, 18222−18227.
(32) Hansen, M. F.; Morup, S. Models for the Dynamics of Interacting Magnetic Nanoparticles. *J. Magn. Magn. Mater.* **1998**, *184*, 262−274.
(33) Lee, J. S.; Tan, R. P.; Wu, J. H.; Kim, Y. K. Effect of Interparticle Interactions and Size Dispersion in Magnetic Nanoparticle Assemblies: A Static and Dynamic Study. *Appl. Phys. Lett.* **2011**, *99*, 06250610.1063/1.3624833
(34) Saikia, K.; Sen, D.; Mazumder, S.; Deb, P. Reassembling Nanometric Magnetic Subunits into Secondary Nanostructures with Controlled Interparticle Spacing. *RSC Adv.* **2015**, *5*, 694−705.
(35) Koenig, S. H.; Kellar, K. E. Theory of 1/T-1 and 1/T-2 Nmrd Profiles of Solutions of Magnetic Nanoparticles. *Magn. Reson. Med.* **1995**, *34*, 227−233.
(36) Jordan, A.; Scholz, R.; Wust, P.; Fahling, H.; Felix, R. Magnetic Fluid Hyperthermia (Mfh): Cancer Treatment with Ac Magnetic Field Induced Excitation of Biocompatible Superparamagnetic Nanoparticles. *J. Magn. Magn. Mater.* **1999**, *201*, 413−419.
(37) Rosensweig, R. E. Heating Magnetic Fluid with Alternating Magnetic Field. *J. Magn. Magn. Mater.* **2002**, *252*, 370−374.
(38) Hergt, R.; Dutz, S. Magnetic Particle Hyperthermia-Biophysical Limitations of a Visionary Tumour Therapy. *J. Magn. Magn. Mater.* **2007**, *311*, 187−192.
(39) Brooks, R. A.; Moiny, F.; Gillis, P. On T-2-Shortening by Weakly Magnetized Particles: The Chemical Exchange Model. *Magn. Reson. Med.* **2001**, *45*, 1014−1020.
(40) LaConte, L. E. W.; Nitin, N.; Zurkiya, O.; Caruntu, D.; O'Connor, C. J.; Hu, X. P.; Bao, G. Coating Thickness of Magnetic Iron Oxide Nanoparticles Affects R-2 Relaxivity. *J. Magn. Reson. Imaging* **2007**, *26*, 1634−1641.

DOI: 10.1021/acsami.6b01377
ACS Appl. Mater. Interfaces 2016, 8, 6953−6961